

# Rotational Raman scattering (Ring effect) in satellite backscatter ultraviolet measurements

Joanna Joiner, Pawan K. Bhartia, Richard P. Cebula, Ernest Hilsenrath, Richard D. McPeters, and Hongwoo Park

A detailed radiative transfer calculation has been carried out to estimate the effects of rotational Raman scattering (RRS) on satellite measurements of backscattered ultraviolet radiation. Raman-scattered light is shifted in frequency from the incident light, which causes filling in of solar Fraunhofer lines in the observed backscattered spectrum (also known as the Ring effect). The magnitude of the rotational Raman scattering filling in is a function of wavelength, solar zenith angle, surface reflectance, surface pressure, and instrument spectral resolution. The filling in predicted by our model is found to be in agreement with observations from the Shuttle Solar Backscatter Ultraviolet Radiometer and the Nimbus-7 Solar Backscatter Ultraviolet Radiometer.

*Key words:* Rotational Raman scattering, satellite ultraviolet.

## 1. Introduction

The filling in of solar Fraunhofer lines, also known as the Ring effect, has been observed in ground-based observations (see, e.g., Grainger and Ring,<sup>1</sup> Harrison and Kendall,<sup>2</sup> Harrison,<sup>3</sup> and Barmore<sup>4</sup>). Several explanations were put forth, including fluorescence and rotational-vibrational Raman scattering, in an attempt to explain these observations. Pure rotational Raman scattering has emerged as the best explanation for the Ring effect (see, e.g., Wallace<sup>5</sup> and Brinkman<sup>6</sup>). Rotational Raman scattering (RRS) has also been observed in the atmospheres of the Jovian planets (see, e.g., Cochran *et al.*<sup>7</sup> and Price<sup>8</sup>). Kattawar *et al.*<sup>9</sup> gave a comprehensive survey of inelastic scattering, including both RRS and Brillouin scattering. The magnitude of the filling in caused by these two types of inelastic scattering was shown to be a function of the input and observed state of polarization, solar zenith angle, and surface reflectivity. The predicted filling in was found to be in qualitative agreement with ground-based observa-

tions. An empirical approach has also been used to characterize the Ring effect at visible wavelengths by the use of ground-based observations in parallel and perpendicular polarizations (Solomon *et al.*<sup>10</sup>).

RRS has also been observed in satellite backscatter ultraviolet (buv) measurements from the continuous scan mode (Park *et al.*<sup>11</sup>) of the Solar Backscatter Ultraviolet (SBUV) radiometer. The RRS filling-in effect on radiances measured with satellite UV ozone-monitoring instruments such as the Total Ozone Mapping Spectrometer (TOMS), SBUV, and SBUV/2 is relatively small (of the order of  $\leq 1\%$ ). Therefore, it has not been accounted for previously in ozone-retrieval algorithms. However, for highly accurate measurements of weakly absorbing species such as SO<sub>2</sub> and NO<sub>2</sub> and for internally consistent ozone measurements at different wavelengths, it is important to have a physical model that can accurately predict RRS effects on buv measurements.

Here we describe a detailed theoretical model that we developed to predict the RRS filling-in effect on buv measurements. The RRS model shows the magnitude of the filling in to be a function of wavelength, instrument spectral resolution, solar zenith angle, surface reflectivity, cloud height, and cloud fraction. We compare the RRS model results with measurements from the Shuttle Solar Backscatter Ultraviolet (SSBUV) Radiometer and the Nimbus-7 SBUV Radiometer in order to validate its spectral characteristics as well as its dependence on solar zenith angle and cloud effects.

---

When this research was performed J. Joiner and R. P. Cebula were with Hughes STX Corporation, Greenbelt, Maryland 20770. J. Joiner, P. K. Bhartia, E. Hilsenrath, and R. D. McPeters are with the Laboratory for Atmospheres, Goddard Space Flight Center, Greenbelt, Maryland 20771.

Received 16 September 1994; revised manuscript received 11 January 1995.

0003-6935/95/214513-13\$06.00/0.

© 1995 Optical Society of America.

## 2. Rotational Raman Scattering

Rayleigh scattering includes both elastic and inelastic scattering that produces multiple lines. The central or Cabannes line consists of the translational Raman spectrum (Brillouin component) and an elastic scattering component, which was called the Gross line by Young.<sup>12</sup> In a single molecular scattering, a fraction,  $f$ , of the scattered intensity is contained in the Cabannes line. The remaining  $1 - f$  of the scattered intensity is contained in the rotational Raman lines. In unpolarized light scattered by diatomic molecules,  $f = \bar{f}_0$ , where  $\bar{f}_0$  is a function of average molecular polarizability  $a$  and the anisotropy of polarizability  $\delta$ , as well as scattering angle  $\Theta$ , and is given by

$$\bar{f}_0 = \frac{(180 + 13\epsilon) + (180 + \epsilon)\cos^2 \Theta}{(180 + 52\epsilon) + (180 + 4\epsilon)\cos^2 \Theta} \quad (1)$$

(Kattawar *et al.*<sup>9</sup>), where  $\epsilon = (\delta/a)^2$ . The value of  $\epsilon$  depends on the scattering molecule as well as on wavelength. Bates<sup>13</sup> developed formalisms to compute  $\epsilon$  for both oxygen and nitrogen as a function of wavelength. His formalisms agree well with laboratory data. Using these formalisms for air, we find that  $\epsilon$  ranges from 0.360 at  $\lambda = 200$  nm to 0.230 at 400 nm. Figure 1 shows  $(1 - \bar{f}_0)$  as a function of  $\Theta$  at  $\lambda = 390$  nm. Figure 2 shows  $(1 - \bar{f}_0)$  as a function of  $\lambda$  at  $\Theta = 0^\circ$ . For photons that have been scattered once or have encountered the ground (or aerosol), it can be assumed that in subsequent scatterings the scattering molecule is illuminated from all directions by unpolarized light (Kattawar *et al.*<sup>9</sup>) In this case  $f = \bar{f}_0$ , where  $\bar{f}_0$  is the solid-angle average of  $\bar{f}_0$  given by

$$\bar{\bar{f}}_0 = \frac{18.0 + 1.0\epsilon}{18.0 + 4.0\epsilon}. \quad (2)$$

In the Earth's atmosphere, the rotational Raman spectrum,  $L(\nu)$ , is given by

$$L(\nu) = \chi_{N_2} L_{N_2}(\nu) + \chi_{O_2} L_{O_2}(\nu) K, \quad (3)$$

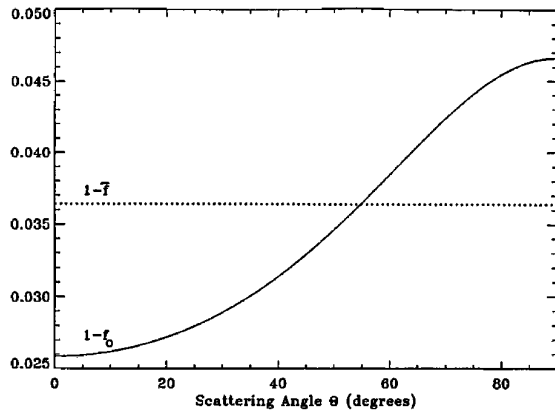


Fig. 1.  $1 - \bar{f}_0$  and  $1 - \bar{\bar{f}}_0$  computed as a function of scattering angle  $\Theta$  at  $\lambda = 390$  nm.

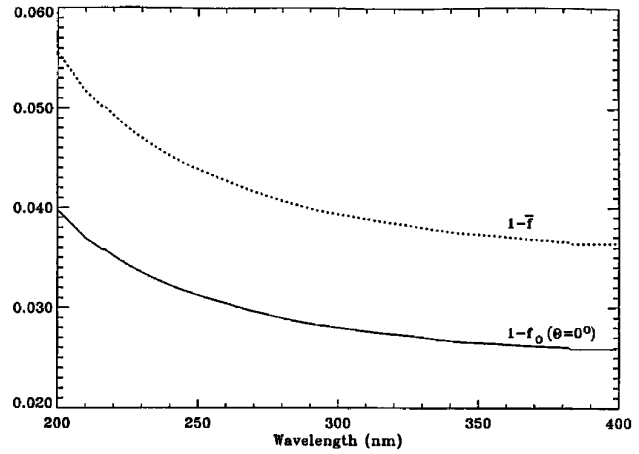


Fig. 2.  $1 - \bar{f}_0$  and  $1 - \bar{\bar{f}}_0$  computed as a function of wavelength at  $\Theta = 0^\circ$ .

where  $\chi_{N_2}$  and  $\chi_{O_2}$  are the mixing ratios of nitrogen and oxygen, respectively, and  $L_{N_2}$  and  $L_{O_2}$  are the normalized RRS spectra of nitrogen and oxygen, respectively. For single-scattered photons,  $K = (1 - \bar{f}_{0,O_2})/(1 - \bar{f}_{0,N_2})$ . For photons scattered more than once or reflected off the ground or cloud, we denote the rotational Raman spectrum as  $\bar{L}(\nu)$ , which we compute by using Eq. (3) with  $K = \bar{K} = (1 - \bar{\bar{f}}_{0,O_2})/(1 - \bar{\bar{f}}_{0,N_2})$ . The variation of  $K$  with scattering angle is relatively small at a given wavelength ( $\sim 4\%$  from  $\Theta = 0^\circ - 90^\circ$ ), and therefore  $\bar{K} \approx K$ . The variation of  $K$  with wavelength is much larger. For example, at  $\Theta = 0^\circ$ ,  $K = 4.7$  at  $\lambda = 200$  nm, and  $K = 2.9$  at  $\lambda = 400$  nm.

The rotational Raman spectrum consists of Stokes and anti-Stokes lines. For Stokes lines,  $J \rightarrow J + 2$  for  $J = 0, 1, 2, \dots$ , where  $J$  is the rotational angular-momentum quantum number of the initial state. The frequency shifts for Stokes lines are approximated with good accuracy by  $\Delta\nu = -(4J + 6)B_0$  (Penny *et al.*<sup>14</sup>), where  $B_0$  is the rotational constant for the ground vibrational state. For anti-Stokes lines,  $J \rightarrow J - 2$  for  $J = 2, 3, 4, \dots$  and  $\Delta\nu = (4J - 2)B_0$ . The relative line strengths,  $L_J$ , are given by

$$L_J = F_J b_{J \rightarrow J'}, \quad (4)$$

where  $F_J$  is the fraction of molecules in the initial state,  $J$ , and  $b_{J \rightarrow J'}$  is the Placzek-Teller coefficient. Here  $F_J$  is approximated accurately by

$$F_J = g_J / (2J + 1) \exp(-E_J/kT), \quad (5)$$

where  $g_J$  is a statistical weight factor that depends on the nuclear spin of the molecule and  $E_J$  is the rotational energy that is approximated by  $J(J + 1)hcB_0$ . For Stokes and anti-Stokes lines,

$$b_{J \rightarrow J+2} = \frac{3(J + 1)(J + 2)}{2(2J + 1)(2J + 3)}, \quad (6)$$

$$b_{J-J-2} = \frac{3(J-1)}{2(2J+1)(2J-1)}, \quad (7)$$

respectively.

Figures 3(a) and 3(b) show  $L_{N_2}(\nu)$  and  $L_{O_2}(\nu)$  at  $\lambda = 390$  nm and at an atmospheric temperature of 273 K. For nitrogen,  $g_J = 6$  and  $g_J = 3$  for even and odd  $J$ , respectively, which gives the alternating line intensities shown in Fig. 3(a). For oxygen,  $g_J = 0$  and  $g_J = 1$  for even and odd  $J$ , respectively, resulting in the absence of even  $J$  lines in Fig. 3(b). Values of  $B_0$  for nitrogen and oxygen, 1.9897 and 1.4378  $\text{cm}^{-1}$ , respectively, are taken from a summary in Penney *et al.*<sup>14</sup> Line strengths  $L_{N_2}(\nu)$ ,  $L_{O_2}(\nu)$ , and  $L(\nu)$  are normalized such that the sum over both the Stokes and anti-Stokes lines is equal to unity. In buv observations, the backscattered radiance is measured at a single wavelength,  $\nu_0$ , and consists of photons that have been elastically scattered and of rotational Raman-scattered photons from a range of frequencies,  $\nu_0 + \Delta\nu_{J-J'}$ . This type of measurement differs slightly from laboratory measurements of rotational Raman spectra in which the scattering molecules are excited at a single frequency,  $\nu_0$ , and observed over a range of Raman-shifted frequencies,  $\nu_0 + \Delta\nu_{J-J'}$ . The relative line strengths in laboratory spectra include a factor  $[(\nu_0 + \Delta\nu_{J-J+\Delta J})/\nu_0]^4$ , whereas  $L_J$  used in Eq. (4) should not include this factor.

### 3. Rotational Raman Scattering Effects on Backscatter Ultraviolet Radiances

Kattawar *et al.*<sup>9</sup> gave a formalism to compute the filled-in spectral response for the ground-based observation of a single isolated Fraunhofer line against a continuum. Their calculation assumed that the frequencies of the rotational Raman lines coincided with the continuum. Therefore, the frequency and intensity variation of the individual rotational Raman lines did not need to be accounted for. In buv observations, however, the Fraunhofer lines are not isolated,

and the rotational Raman line structure must be included in the computation of the filling in. We have therefore developed a formalism to include the spectral and intensity distribution of the rotational Raman lines described above.

To quantify the RRS effect on buv radiances, we define the filling-in factor,  $k(\lambda_0)$ , to be

$$k(\lambda_0) = \frac{I_m(\lambda_0) - \int I_R(\lambda)B(\lambda - \lambda_0)d\lambda}{\int I_R(\lambda)B(\lambda - \lambda_0)d\lambda} = \frac{I_m(\lambda_0) - \bar{I}_R(\lambda_0)}{\bar{I}_R(\lambda_0)}, \quad (8)$$

where  $I_m(\lambda_0)$  is the measured radiance at effective wavelength  $\lambda_0$ ,  $I_R(\lambda)$  is the monochromatic radiance calculated by the use of traditional (elastic) Rayleigh scattering models,  $B(\lambda - \lambda_0)$  is the instrument band-pass, and  $\bar{I}_R(\lambda_0)$  can be thought of as the slit-averaged computed radiance. In the following sections we compute  $k$  by using increasingly complex models of atmospheric scattering, starting with a single-scattering model. We do not include the effects of aerosols except in the case of clouds, which are modeled simply as a Lambertian reflecting layer. In this study we treated the Cabannes line, including the Brillouin component, as a single line (i.e., we ignored Brillouin scattering). We simulated the effect of Brillouin scattering by using a rough shape of the Brillouin spectrum from Kattawar *et al.*<sup>9</sup> We found the Brillouin contribution to be negligible (a filling-in factor of less than 0.01%) in all cases.

#### A. Single-Scattering Model

In the simplified case of single-scattering,  $I_R(\lambda)$  can be computed according to

$$I_R(\lambda) = F(\lambda)P(\Theta, \lambda) \times \int_{p_0}^{\infty} \exp[-\alpha(\lambda)Sx(p) - \beta(\lambda)Sp]dp, \quad (9)$$

where  $F(\lambda)$  is the solar flux,  $P(\Theta, \lambda)$  is the phase function for an isotropic Rayleigh scatterer (which has a small wavelength dependence caused by the wavelength dependence of  $\epsilon$ ),  $\alpha$  is the ozone absorption coefficient per unit ozone amount,  $\beta$  is the Rayleigh scattering coefficient per unit pressure,  $S$  is the slant path or geometrical path defined as the  $\sec(\theta_0) + \sec(\theta)$ , where  $\theta_0$  is the solar zenith angle and  $\theta$  is the satellite zenith angle, and  $x(p)$  is the column amount of ozone above pressure  $p$ . Note that for nadir-viewing instruments, scattering angle  $\Theta$  is equal to  $\pi$  minus  $\theta_0$ . Because  $P(\Theta, \lambda)$  is of the form  $a + b \cos^2 \Theta$ ,  $P(\Theta, \lambda) = P(\theta_0, \lambda)$ . Likewise from Eq. (1),

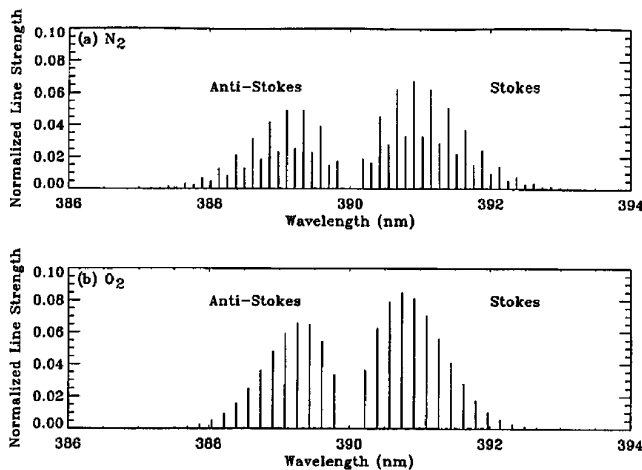


Fig. 3. Rotational Raman line strengths  $L$  (normalized such that the sum over all lines is equal to unity) for (a)  $N_2$  and (b)  $O_2$  for radiance measured at  $\lambda = 390$  nm and  $T = 273$  K.

$f_0(\Theta) = f_0(\theta_0)$ . The measured radiance is given by

$$I_m(\lambda_0) = \int f_0(\lambda) I_R(\lambda) B(\lambda - \lambda_0) d\lambda + \int \left\{ \int [1 - f_0(\lambda')] L(\lambda - \lambda') I_R(\lambda') d\lambda' \right\} \times B(\lambda - \lambda_0) d\lambda, \quad (10)$$

where  $L(\lambda)$  is the complete rotational Raman spectrum of air, including both Stokes and anti-Stokes lines as outlined in Section 2. The first term in Eq. (10) represents photons in the Cabannes line that have not been Raman scattered from the incident wavelength. The second term in Eq. (10) represents photons that have been Raman scattered to the wavelength of observation from wavelengths shifted by amounts appropriate for Stokes and anti-Stokes lines. Because the variation of  $f_0(\lambda)$  with  $\lambda$  is small for typical instrument bandpass (FWHM of approximately 1 nm or less), Eq. (10) can be written as

$$I_m(\lambda_0) = f_0(\lambda_0) \int I_R(\lambda) B(\lambda - \lambda_0) d\lambda + [1 - f_0(\lambda_0)] \int \left[ \int L(\lambda - \lambda') I_R(\lambda') d\lambda' \right] \times B(\lambda - \lambda_0) d\lambda. \quad (11)$$

Alternatively,  $I_m(\lambda_0)$  can be written as

$$I_m(\lambda_0) = [C_1(\lambda_0) I_R(\lambda_0)] B(-\lambda_0) = C_1(\lambda_0) [I_R(\lambda_0) B(-\lambda_0)] = C_1(\lambda_0) \bar{I}_R(\lambda_0), \quad (12)$$

where  $\bar{I}_R(\lambda_0)$  denotes convolution. Here  $C_1(\lambda_0)$  is given by

$$C_1(\lambda_0) = f_0(\lambda_0) \delta(\lambda_0) + [1 - f_0(\lambda_0)] L(\lambda_0), \quad (13)$$

where  $\delta(\lambda_0)$  is the unit impulse function and the subscript 1 denotes single scattering. Substituting in Eq. (8) gives

$$k_1(\lambda_0) = \frac{C_1(\lambda_0) \bar{I}_R(\lambda_0)}{I_R(\lambda_0)} - 1. \quad (14)$$

Note that the filling in caused by RRS results not only from the Fraunhofer structure in the solar spectrum but also from atmospheric absorption. In the Earth's atmosphere, the strong wavelength-dependent ozone absorption in the UV bands can cause a small amount of filling in. However, if the atmospheric transmission is relatively constant with wavelength, the filling-in factor may be computed as described above by the substitution of solar irradiance  $F(\lambda)$  in place of  $I_R(\lambda)$ . In this case it is not necessary to compute the filled-in response at high resolution and then to convolve the result with the instrument function. In fact, one obtains the best

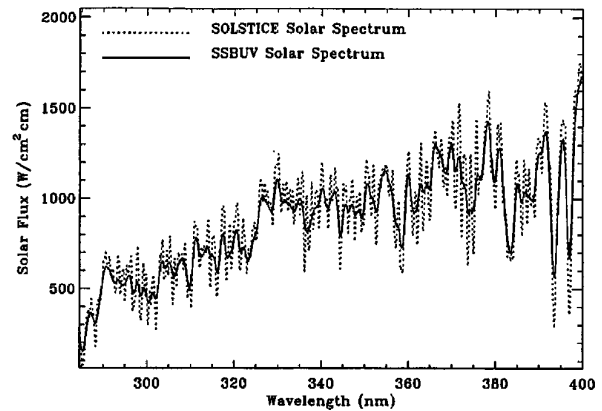


Fig. 4. Measured solar irradiance from the SOLSTICE and SSBUV instruments as a function of wavelength.

results by computing the filling in by using a solar spectrum observed with the same instrument at the same resolution as the observed backscattered spectrum, i.e., by replacing  $\bar{I}_R$  by  $\bar{F}$  in Eq. (14).

In Fig. 4 the dotted curve shows a solar spectrum taken with the solar-stellar irradiance comparison experiment (SOLSTICE) instrument (Rottman *et al.*<sup>15</sup> and Woods *et al.*<sup>16</sup>). The SOLSTICE resolution shown in Fig. 4 is 0.2 nm, and the average wavelength step spacing is approximately 0.089 nm. The solid curve shows an SSBUV solar spectrum. The resolution of the SSBUV spectrum is approximately 1.1 nm. The deepest Fraunhofer lines in this region of the spectrum are the calcium II K and H lines at 393.37 and 396.85 nm. Other strong lines include the Mg I line at 285.21 nm and the Fe I (a blend) line near 358 nm. Figure 5 shows  $k_1(\lambda_0)$  (in percent) from 280 to 400 nm computed at the SOLSTICE resolution for  $\theta_0 = 45^\circ$  (dotted curve) and at the SSBUV resolution also for  $\theta_0 = 45^\circ$  (solid curve). The structure in  $k_1(\lambda_0)$  is anticorrelated with  $F(\lambda_0)$  because of both the filling of Fraunhofer lines and the depleting of peaks in  $F(\lambda_0)$ . Negative values represent depletion rather than filling in. The magnitude of the filling in is

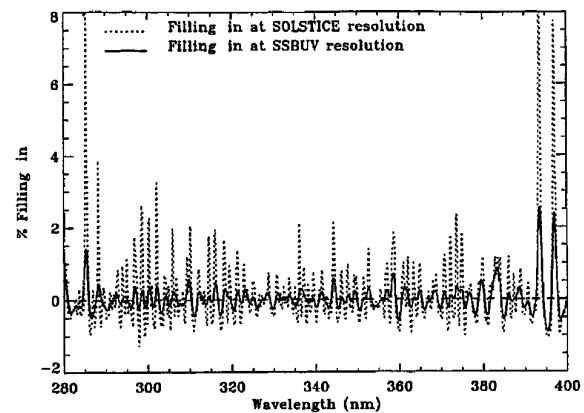


Fig. 5. Single-scatter filling in,  $k_1$ , as a function of wavelength computed at the SOLSTICE and SSBUV resolutions for solar zenith angle  $\theta_0 = 45^\circ$ .

smaller at lower resolution, because bandpass averaging over a larger bandpass or slit has the effect of decreasing the strength of the Fraunhofer lines. The filling in was computed with an atmospheric temperature of 273 K (as will be done in following calculations). The effect of temperature on the filling in is small ( $\Delta k/\Delta T \approx 0.0042\%/K$ ). The purpose of Fig. 5 is to illustrate the dependence of the filling in on instrument spectral resolution. Therefore, we neglected the filling in caused by absorption in the Earth's atmosphere. The main effect of including terrestrial absorption is at wavelengths between 300 and 340 nm, where the radiance changes rapidly with wavelength. Figure 6 shows the filling in computed with and without terrestrial absorption at the SSBUV resolution from 300 to 340 nm.

#### B. Multiple-Scattering Model without Reflection

For multiple scattering without reflection,  $\bar{I}_R(\lambda)$  is given by

$$\bar{I}_R(\lambda) = \sum_{n=1}^{\infty} \bar{I}_n(\lambda), \quad (15)$$

where  $\bar{I}_n(\lambda)$  is the component of the total backscattered intensity from the  $n$ th scattering. In this case, if we drop the  $(\lambda_0)$  in the notation,  $k(\lambda_0)$  is given by

$$k = k_1 \frac{\bar{I}_1}{\bar{I}_R} + \sum_{n=2}^{\infty} \bar{k}_n \frac{\bar{I}_n}{\bar{I}_R}, \quad (16)$$

where  $\bar{k}_n$  is the filling in caused by photons that have undergone  $n$  scattering events. Here  $\bar{k}_n$  is given by

$$\bar{k}_n = \frac{\bar{C}_n * \bar{I}_R}{\bar{I}_R} - 1, \quad (17)$$

where  $\bar{C}_n$  is  $\bar{C}_1$  convolved with itself  $n - 1$  times. For example, in the case of  $n = 2$ ,

$$\begin{aligned} \bar{C}_2(\lambda_0) &= \bar{C}_1(\lambda_0) * \bar{C}_1(\lambda_0) = \bar{f}_0^2 \delta(\lambda_0) + 2\bar{f}_0(1 - \bar{f}_0)\bar{L}(\lambda_0) \\ &+ (1 - \bar{f}_0)^2 [\bar{L}(\lambda_0) * \bar{L}(\lambda_0)], \end{aligned} \quad (18)$$

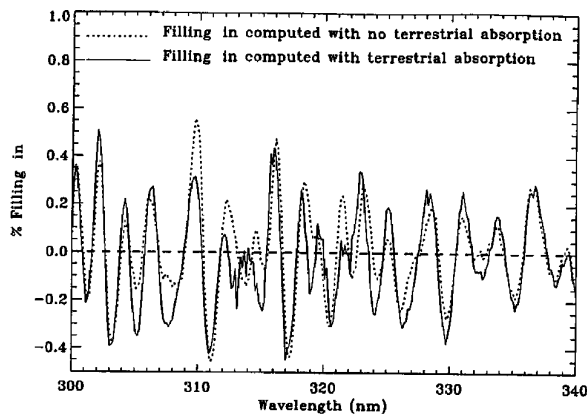


Fig. 6. Single-scatter filling in computed with and without terrestrial absorption as a function of wavelength at the SSBUV resolution.

where  $\bar{f}_0$  is the solid-angle average of  $f_0$  defined earlier. The second term in Eq. (18) represents photons that have been Raman scattered once into the observed wavelength. The last term in Eq. (18) represents photons that have been Raman scattered twice. The wavelength shifts of second-order rotational Raman-scattered photons can therefore be as large as twice the wavelength shifts from first-order Raman-scattered photons. The fraction of photons that have been Raman scattered twice into the wavelength of observation from the far Raman wings is small because of the  $(1 - \bar{f}_0)^2$  factor. In fact, one can simplify Eq. (16) by neglecting higher-order terms in  $(1 - \bar{f}_0)$ . In this case,  $k_2$  simplifies to

$$\begin{aligned} \bar{k}_2 &\approx \frac{[2\bar{f}_0\delta(\lambda_0) + 2(1 - \bar{f}_0)\bar{L}(\lambda_0) - \delta(\lambda_0)] * \bar{I}_R}{\bar{I}_R} - 1 \\ &= \frac{2\bar{C}_1(\lambda_0) * \bar{I}_R}{\bar{I}_R(\lambda_0)} - 2 = 2\bar{k}_1. \end{aligned} \quad (19)$$

Using the same approximation, we find that

$$\bar{k}_n \approx n\bar{k}_1, \quad (20)$$

$$k = k_1 \frac{\bar{I}_1}{\bar{I}_R} + \bar{k}_1 \sum_{n=2}^{\infty} n \frac{\bar{I}_n}{\bar{I}_R}. \quad (21)$$

Note that because  $\bar{C}_1$  depends on  $\bar{I}_R$  and  $\bar{f}_0$ ,  $\bar{C}_1$  for the multiple-scattering case is not the same as  $C_1$  for the single-scattering case. We have used a radiative transfer model based on successive iteration of the auxiliary equation (Dave<sup>17</sup>) in a pseudospherical atmosphere (DeLuisi and Mateer<sup>18</sup>) to compute the normalized backscattered intensities,  $I_n$  (caused by unit solar flux) at every iteration or order of scattering for a given wavelength, solar zenith angle, satellite scan angle (we assumed nadir view for all calculations), and surface pressure. In the radiative transfer model, the atmosphere is divided into thin shells for the incoming and outgoing rays. For intermediate higher orders of scattering, a plane-parallel atmosphere approximation is used. Recent calculations by Caudill<sup>19</sup> show that total intensities computed by the use of a full spherical radiative transfer model agree with the pseudospherical radiative transfer model to within  $\sim 0.2\%$  for nadir-viewing observations with solar zenith angles up to  $88^\circ$  at the wavelengths that are used here. In the radiative transfer calculation, a temperature and ozone profile are specified. At each wavelength the Rayleigh scattering coefficient and effective ozone absorption coefficient are also specified.

Equations (16) and (21) can be thought of as taking a weighted average of the filling in over all components of the radiance. We evaluated the summations in Eqs. (16) and (21) up to 8 orders of scattering. The last order contains the intensities of all higher orders of scattering. Table 1 gives values of  $I_n/\bar{I}_R$  for  $n = 1, 2, 3$ , and  $4 \dots \infty$  at  $\theta_0 = 0^\circ, 45^\circ, 81^\circ$ , and  $88^\circ$  for  $\lambda = 360$  nm and  $\lambda = 393$  nm. Most of the total

Table 1.  $I_n/I_R(\%)$  for  $\lambda = 360$  nm and  $\lambda = 393$  nm

$n$	$\theta_0 (\lambda = 360 \text{ nm})$				$\theta_0 (\lambda = 393 \text{ nm})$			
	0°	45°	81°	88°	0°	45°	81°	88°
1	60.5	58.0	56.3	59.9	67.9	66.0	63.8	66.2
2	23.4	23.7	23.2	21.7	21.5	22.0	22.3	21.0
3	9.4	10.1	10.6	9.6	7.0	7.7	8.4	7.8
4...∞	6.7	8.2	9.9	8.8	3.6	4.3	5.5	5.0

backscattered intensity results from the first scattering. The fraction of the total intensity in the higher orders of scattering is greater at 360 nm because of the  $\lambda^{-4}$  dependence of Rayleigh scattering. The fraction of the total intensity contained in the higher orders of scattering increases with solar zenith angle up to 81°, but it then begins to decrease at higher solar zenith angles.

Figure 7 shows  $k_1$  (solid curve),  $\bar{k}_1$  (dotted curve), and  $k$  (dashed curve) as a function of solar zenith angle at 393 nm near the center of the Ca K line at SSBV resolution. There are two effects that contribute to the solar zenith angle dependence of  $k$ . In the first term of Eq. (21), the single-scattering dependence of  $k_1$  on  $\theta_0$  is due to  $f_0$  in Eq. (1). In the second term of Eq. (21),  $k_1$  has no solar zenith angle dependence from  $f_0$ , but the intensity distribution over the orders of scattering varies slightly with  $\theta_0$ . The single-scattering effect is responsible for the majority of the solar zenith angle dependence. The main effect of the higher orders of scattering is to increase the filling in, although the solar zenith angle dependence is slightly smaller for  $k$  than for  $k_1$ . The next subsection extends the above model to include the effects of surface reflection.

### C. Multiple-Scattering Model with Reflection

In the presence of a Lambertian reflecting surface with reflectivity  $R$ , the normalized backscattered intensity,  $\bar{I}_R$ , at solar zenith angle  $\theta_0$  ( $\mu_0 = \cos \theta_0$ )

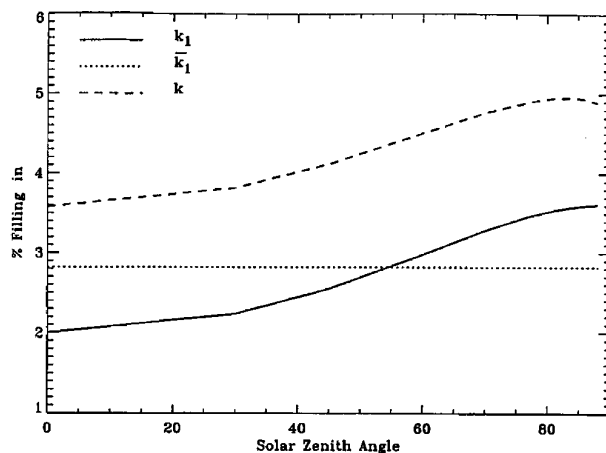


Fig. 7. Single-scatter filling in,  $k_1$ , computed at  $\lambda = 393$  nm as a function of solar zenith angle; solid-angle average of single-scatter filling in,  $\bar{k}_1$ , and filling in at  $\lambda = 393$  nm,  $k$ , including effects of multiple scattering and excluding surface-reflection effects.

observed at the top of the atmosphere with satellite zenith angle  $\theta$  ( $\mu = \cos \theta$ ) is given by

$$\begin{aligned} \bar{I}_R &= \bar{I}_R(R=0) + RI_g(\mu_0)\gamma(\mu) + R^2 I_g(\mu_0)\gamma(\mu)S_b \\ &\quad + R^3 I_g(\mu_0)\gamma(\mu)S_b^2 + \dots \\ &= \bar{I}_R(R=0) + \frac{RI_g(\mu_0)\gamma(\mu)}{1 - RS_b}, \end{aligned} \quad (22)$$

where  $I_g(\mu_0)$  is the total radiance reaching the surface,  $\gamma(\mu)$  is the transmittance of the radiance reflected from the surface, and  $S_b$  is the component of the reflected surface radiance that is reflected by the atmosphere back to the surface. Both  $I_g(\mu_0)$  and  $\gamma(\mu)$  can be expressed as the sum of direct and diffuse components. The product of  $I_g$  and  $\gamma$  is then given by

$$\begin{aligned} I_g(\mu_0)\gamma(\mu) &= [\mu_0 \exp(-\tau_0/\mu_0) + g][\exp(-\tau/\mu) + t] \\ &= \mu_0 \exp(-\tau_0/\mu_0)\exp(-\tau/\mu) \\ &\quad + \mu_0 \exp(-\tau_0/\mu_0)t + g\exp(-\tau/\mu) + gt, \end{aligned} \quad (23)$$

where  $\mu_0 \exp(-\tau_0/\mu_0)$  and  $g$  are the direct and diffuse components of  $I_g(\mu_0)$  respectively, and  $\exp(-\tau/\mu)$  and  $t$  are the direct and diffuse components of  $\gamma(\mu)$ , respectively. We used the above-mentioned radiative transfer model to compute the intensities of  $t$ ,  $g$ , and  $S_b$  in addition to  $I_R(R=0)$  at every order of scattering.

The filling factor, including the effects of multiple scattering and surface reflection, is given by

$$\begin{aligned} k &= \frac{k(R=0)\bar{I}_R(R=0)}{\bar{I}_R} + \frac{R}{\bar{I}_R} \\ &\times \left\{ \sum_{n=1}^{\infty} \bar{k}_n [g_n \exp(-\tau/\mu) + t_n \mu_0 \exp(-\tau_0/\mu_0)] \right. \\ &\quad + \sum_{n_1=1}^{\infty} \sum_{n_2=1}^{\infty} \bar{k}_{n_1+n_2} g_{n_1} t_{n_2} \left. \right\} + \frac{R^2}{\bar{I}_R} \\ &\times \left\{ \sum_{n_1=1}^{\infty} \sum_{n_2=1}^{\infty} \bar{k}_{n_1+n_2} [g_{n_1} S_{bn_2} \exp(-\tau/\mu) \right. \\ &\quad + t_{n_1} S_{bn_2} \mu_0 \exp(-\tau_0/\mu_0)] \\ &\quad + \sum_{n_1=1}^{\infty} \sum_{n_2=1}^{\infty} \sum_{n_3=1}^{\infty} \bar{k}_{n_1+n_2+n_3} g_{n_1} t_{n_2} S_{bn_3} \\ &\quad + \sum_{n=1}^{\infty} \bar{k}_n S_{bn} \exp(-\tau/\mu) \mu_0 \exp(-\tau_0/\mu_0) \left. \right\} + \dots, \end{aligned} \quad (24)$$

where the subscripts on  $S_b$ ,  $g$ ,  $t$  denote the order of scattering. We can simplify Eq. (24) by using the

approximations given in the last subsection. Then

$$k \simeq \frac{k(R=0)\bar{I}_R(R=0)}{\bar{I}_R} + \frac{\bar{k}_1}{\bar{I}_R} [RI_g\gamma n_R + R^2I_g\gamma S_b(n_R + n_b) + R^3I_g\gamma S_b^2(n_R + 2n_b) + \dots], \quad (25)$$

where

$$n_b = \sum_{n=1}^{\infty} \frac{nS_{bn}}{S_b}, \quad (26)$$

$$n_R = \frac{n_g g \exp(-\tau/\mu) + n_t \mu_0 \exp(-\tau/\mu_0) + n_{gt} g t}{I_g(\mu_0)\gamma(\mu)}, \quad (27)$$

$$n_g = \sum_{n=1}^{\infty} \frac{n g_n}{g}, \quad (28)$$

$$n_t = \sum_{n=1}^{\infty} \frac{n t_n}{t}, \quad (29)$$

$$n_{gt} = \sum_{n_1}^{\infty} \sum_{n_2=1}^{\infty} \frac{(n_1 + n_2)(g_{n_1} t_{n_2})}{g t} = n_g + n_t. \quad (30)$$

Equation (25) may now be written in closed form according to

$$k = \frac{k(R=0)\bar{I}_R(R=0)}{\bar{I}_R} + \frac{\bar{k}_1}{\bar{I}_R} \left[ \frac{RI_g\gamma n_R}{1 - RS_b} + \frac{R^2I_g\gamma S_b n_b}{(1 - RS_b)^2} \right]. \quad (31)$$

Table 2 gives  $t_n/t$ ,  $S_{bn}/S_b$ , and  $g_n/g$  for  $n = 1, 2, 3$  and  $n = 4 \dots \infty$  at  $\lambda = 393$  nm for  $\theta_0 = 0^\circ, 45^\circ, 81^\circ$ , and  $88^\circ$  ( $t_n/t$  and  $S_{bn}/S_b$  remain constant with  $\theta_0$ ). Table 3 lists  $I_n/I_R(R=0)$ ,  $t_n/t$ ,  $S_{bn}/S_b$ , and  $g_n/g$  for  $n = 1, 2, 3$  and  $n = 4 \dots \infty$  for  $\lambda = 393$  nm,  $\theta_0 = 45^\circ$ , and surface pressures of 0.6 and 0.3 bar. The intensity distribution is seen to shift toward lower orders of scattering as the surface pressure decreases. Table 4 gives  $I_R(R=0)$ ,  $I_g\gamma$ ,  $S_b$ ,  $\mu_0 \exp(-\tau_0/\mu_0)$ ,  $\exp(-\tau/\mu)$ ,  $g$ , and  $t$  for  $\theta_0 = 0^\circ, 45^\circ, 81^\circ$ , and  $88^\circ$  at  $\lambda = 393$  nm and surface pressure of 1 bar.

Table 2.  $t_n/t$ ,  $S_{bn}/S_b$ , and  $g_n/g$  (%) for  $\lambda = 393$  nm

$n$	$t_n/t$	$S_{bn}/S_b$	$g_n/g$ : $\theta_0$			
			$0^\circ$	$45^\circ$	$81^\circ$	$88^\circ$
1	64.8	63.1	64.8	61.7	56.9	55.3
2	22.5	22.6	22.5	23.4	25.0	25.6
3	8.0	8.6	8.0	9.0	10.5	11.1
4... $\infty$	4.7	5.7	4.7	5.9	7.6	8.0

Table 3.  $I_n/I_R(R=0)$ ,  $t_n/t$ ,  $S_{bn}/S_b$ , and  $g_n/g$  (%) for  $\lambda = 393$  nm,  $\theta_0 = 45^\circ$ , and Surface Pressure  $P = 0.6$  and  $P = 0.3$

$n$	$P = 0.6$				$P = 0.3$			
	$I_n/I_R$	$t_n/t$	$S_{bn}/S_b$	$g_n/g$	$I_n/I_R$	$t_n/t$	$S_{bn}/S_b$	$g_n/g$
1	75.3	72.3	74.7	72.1	84.7	82.2	84.4	82.5
2	18.4	19.7	18.7	19.9	12.9	14.5	13.1	14.3
3	4.7	5.6	4.8	5.7	2.0	2.7	2.1	2.6
4... $\infty$	1.6	2.4	1.8	2.3	0.4	0.6	0.4	0.6

From Table 4 one can compute the radiance from each term in Eq. (22). For low reflectivities, the majority of the total backscattered radiation is due to the  $\bar{I}_R(R=0)$  term (approximately 70–90% of the total, depending on solar zenith angle), and all terms involving  $S_b$  are negligible (contribute less than 1% to the total). At high reflectivities, the  $RI_g\gamma$  term in Eq. (22) becomes the major contributor of the total radiance, contributing approximately 50–70% of the total radiance. At high reflectivities the  $\bar{I}_R(R=0)$  term drops to less than 35% of the total radiance and the terms involving  $S_b$  become significant, with the first  $S_b$  term contributing 12–15% of the total radiance. The main change in the intensity distribution with solar zenith angle is in  $\mu_0 \exp(-\tau_0/\mu_0)$ . At low solar zenith angles,  $\mu_0 \exp(-\tau_0/\mu_0)$  represents  $\sim 80\%$  of  $I_g(\mu_0)$ , whereas at high solar zenith angles it contributes only  $\sim 20\%$  of  $I_g(\mu_0)$ .

In Eqs. (21) and (31), the filling-in factor is seen to increase with the average number of scatterings. As described above, the average number of scatterings depends on several factors, including solar zenith angle, surface reflectivity, and pressure of the reflecting layer. Figure 8 shows the filling in,  $k$ , at 393 nm computed as a function of solar zenith angle for surface reflectivities of 95%, 20%, and 8% at a surface pressure of 1 bar. A 95% reflectivity is a good approximation of reflectivities observed over ice. A 20% reflectivity approximates that observed over old snow. A reflectivity of 8% is indicative of ocean and land that is not covered with snow or ice. At the low solar zenith angles, the filling in decreases with increasing reflectivity. In this case the direct components of  $I_g$  and  $\gamma$  (which undergo no molecular scattering) increase with reflectivity, thereby decreasing the filling in. However, at high solar zenith angles the filling in increases with increasing reflectivity, because of an increase in the average number of scatterings. The increase in the number of scatterings results both from an increase in the reflected diffuse component and from multiple reflections between the surface and atmosphere. Figure 9 shows the filling in at 393 nm as a function of solar zenith angle, but for a surface reflectivity of 80% (indicative of clouds) at surface pressures of 1.0, 0.6, and 0.3 bar. As expected, the magnitude of the filling in decreases with decreasing surface pressure (increasing cloud height) as the average number of scatterings decreases. The filling-in factors in Figs. 8 and 9 were computed

Table 4. Components of  $I_R$  for Unit Solar Flux at  $\lambda = 393$  nm

$\theta$ (deg)	$I_R(R=0)$	$I_g\gamma$	$S_b$	$\mu_0 \exp(-\tau_0/\mu_0)$	$\exp(-\tau/\mu)$	$g$	$t$
0	0.0473	0.2230	0.2482	0.2164	0.6797	0.0501	0.1573
45	0.0341	0.1478	0.2482	0.1305	0.6797	0.0461	0.1573
81	0.0126	0.0213	0.2482	0.0047	0.6797	0.0208	0.1573
88	0.0044	0.0052	0.2482	0.00001	0.6797	0.0062	0.1573

by the use of the simplified formalism in Eq. (31). The simplifying assumptions in Eq. (31) can result in errors of the order of 5–10% of the total filling in. Therefore, in the following comparisons with observations, we compute the filling in by using the more exact formalism given by Eq. (24).

#### 4. Comparison with Observations

To validate various aspects of the RRS model, we compared the predicted filling in with observations from the SSBUV and SBUV radiometers. The SSBUV radiometer, which flies on the space shuttle, is the refurbished engineering model of SBUV/2. The primary mission of the SSBUV radiometer is to provide regular calibration checks of SBUV/2 instruments, which fly routinely on NOAA satellites, and of TOMS instruments, which fly on NASA satellites. Both the SBUV and SSBUV radiometers are nadir-viewing instruments. The nominal field of view of both instruments is  $11.3^\circ \times 11.3^\circ$ . For the shuttleborne SSBUV radiometer, this translates into an instantaneous field of view (IFOV) of approximately 50 km. For the Nimbus-7 SBUV radiometer, the IFOV is approximately 200 km. The SSBUV and SBUV fields of view move approximately 7.6 km/s and 6 km/s, respectively. The SSBUV instrument is a double-grating monochromator, which covers wavelengths between 160 and 405 nm with a spectral resolution of approximately 1.1 nm. The SSBUV instrument also includes a coaligned cloud-cover radiometer (CCR), which has a central wavelength of 379 nm and a spectral resolution of 3 nm.

The first optical element in the Earth-view mode is a depolarizer that reduces the polarization sensitivity of the instrument to less than 2%. Kattawar *et al.*<sup>9</sup> showed that the magnitude of the filling in is different for polarized and depolarized light. All calculations were made for depolarized light. Polarization effects on observations should be negligible, except in the case of horizontal polarization at solar zenith angles greater than  $\sim 70^\circ$ . For example, the observed filling in at a solar zenith angle of  $90^\circ$ , assuming a 2% sensitivity to horizontal polarization, would increase by  $\sim 20\%$ .

Observations of the filling-in effect were taken in two different operating modes of the SSBUV instrument: the sweep mode and the discrete mode. In the sweep mode, measurements are made that cover the full wavelength range of the instrument in nominal steps of 0.148 nm. The integration time is 0.1 s for each step. The CCR makes one observation for every ten monochromator observations in the sweep mode (integration time 1 s). A full spectral scan, including retrace, takes 192 s. In the discrete mode, the SSBUV instrument is programmed to make repeated observations at 12 preselected wavelengths. In this mode the monochromator integration time is 1.25 s at each wavelength, followed by 0.75 s in which the grating is rotated to the next position. Following the 12th wavelength measurement, the grating takes 8 s to rotate back to the initial starting position. A complete scan, including retrace, therefore takes 32 s. In the discrete mode, the CCR integration time is 1.25 s and is fully synchronized with the integration of the monochromator. The SSBUV instrument

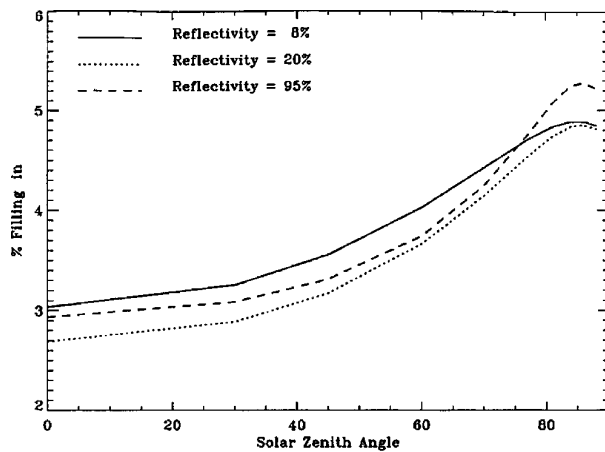


Fig. 8. Computed filling in,  $k$ , including multiple-scattering and surface-reflection effects as a function of solar zenith angle at the SSBUV resolution with  $\lambda = 393$  nm, surface pressure of 1.0 bar, and reflectivities of 8%, 20%, and 95%.

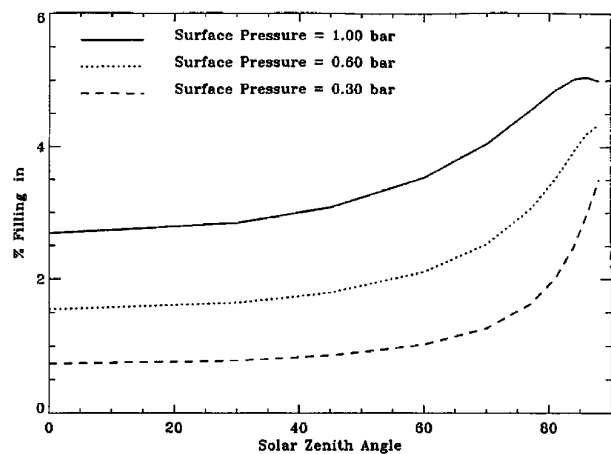


Fig. 9. Computed filling in,  $k$ , as a function of solar zenith angle at the SSBUV resolution with  $\lambda = 393$  nm, reflectivity of 80%, and surface (cloud top) pressures of 1.0, 0.6, and 0.3 bar.



deploys a transmission diffuser in front of its entrance aperture to make normal-incidence solar irradiance measurements. Solar irradiance measurements were obtained in each of the two operating modes described above. The SBUV instrument, which flew on the Nimbus-7 satellite, is very similar to the SSBUV instrument. It has been described in detail by McPeters<sup>20</sup> and references therein.

There are three main sources of error that affect SSBUV measurements in both of the two modes described above. The statistical precision of a single SSBUV measurement is typically of the order of 0.1–0.2% ( $1\sigma$ ) and at worst slightly less than 1%, which occurs at the low end of the electronic gain range used for the most intense radiance signals. These estimates are based on the analysis of solar irradiance measurements (Hilsenrath *et al.*<sup>21</sup> and Cebula *et al.*<sup>22</sup>). Another source of error is due to small wavelength shifts between the Earth radiance and solar irradiance measurements. The analysis of solar irradiance measurements show the scan-to-scan wavelength repeatability to be of the order of 0.02 nm, which results in a radiance accuracy of at worst 0.18%. However, systematic wavelength drifts as large as  $\Delta\lambda = \pm 0.04$  nm have been observed within a single flight. The wavelength drifts were shown to be roughly correlated with temperature excursions experienced during the flights. As we show below, wavelength shifts of this magnitude can result in significant errors at some wavelengths. A third source of error results from the inability to correct completely for scene changes that occur as the instrument field of view moves during the time it takes to complete a measurement. Because the SSBUV field of view changes rapidly because of its low orbit, scene changes can result in significant errors.

We can estimate the combined error resulting from the three sources described above by examining the ratio of the radiance measured by the CCR to the coincident radiance measured at a monochromator wavelength not affected by RRS. For this comparison, we used two different discrete wavelengths near 360 nm and 393 nm where the predicted RRS filling in was close to zero. After correcting for the difference in radiance caused by Rayleigh scattering (not including RRS), we found the standard deviation of the ratio of the CCR to the discrete wavelength radiance to be approximately 2.5% for both discrete wavelengths. As described above, this error is much larger than that expected from radiance or wavelength precision. Therefore, most of the error may be attributed to the inability to correct completely for scene changes.

It should be noted that small differences in the spectral resolution between the observed radiance and irradiance can create a residual in the radiance-to-irradiance ratio, which resembles the filling in caused by rotational Raman scattering. Although this effect has sometimes been referred to as the Ring effect, it has nothing to do with rotational Raman or other types of scattering. For our observations, the instru-

ment field of view was fully illuminated for both the solar and Earth measurements so that the spectral resolution was identical for both the observed radiance and irradiance.

#### A. Wavelength Dependence

We first examine the spectral dependence of the filling in by using SSBUV Earth and solar view data that was obtained in the sweep mode during two orbits of shuttle flight STS-56 in April 1993. A total of 26 complete Earth sweep scans were made at solar zenith angles between 50° and 95°. Several solar sweep measurements were made throughout the flight both before and after the Earth-view measurements.

We restrict our study to longer wavelengths that are insensitive to ozone absorption (i.e.,  $\lambda_0 > 350$  nm). However, these wavelengths are sensitive to changes in cloud cover, surface reflectivity, and solar zenith angle as the instrument field of view moves. To account for scene changes, we interpolated CCR radiances to coincide with each step of the monochromator sweep measurement. The normalized radiance (radiance divided by the solar irradiance) at each sweep step was then divided by the interpolated CCR radiance, resulting in what we refer to as corrected radiance  $N(\lambda_0)$ . Because the corrected radiance, neglecting the filling-in effect, is a smooth function of wavelength between 350 and 400 nm, a second-order polynomial,  $Q(\lambda_0)$ , can be fit to it. Then the observed filling in,  $k^{ob}(\lambda_0)$ , is approximately equal to  $[N(\lambda_0) - Q(\lambda_0)]/Q(\lambda_0)$ .

Initial comparisons showed an apparent wavelength shift of approximately 0.2–0.4 nm between the observed and computed filling in. The cause of this apparent wavelength shift was traced to a much smaller wavelength shift (0.02–0.03 nm) between the radiance and solar irradiance used to derive  $k^{ob}(\lambda_0)$ . As described above, systematic wavelength shifts of this magnitude can occur in the SSBUV instrument. Figure 10 shows the computed filling in,  $k^c$  (solid curve), at a solar zenith angle of 88°. Also shown is

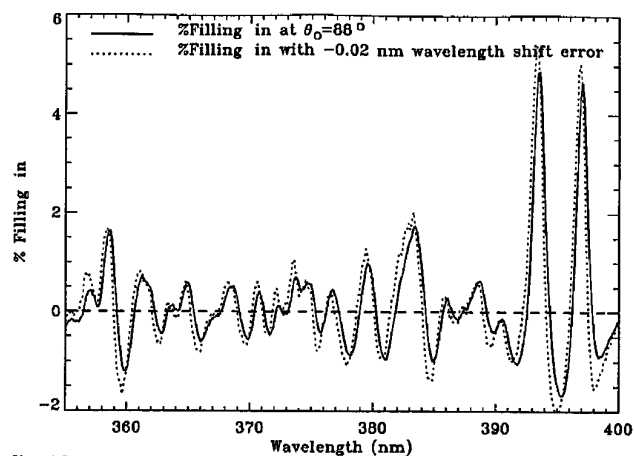


Fig. 10. Computed filling in,  $k^c$ , at  $\theta_0 = 88^\circ$ , and computed filling in,  $k_{\Delta\lambda}$ , with error caused by a wavelength shift of  $-0.02$  nm between radiance and irradiance scans.

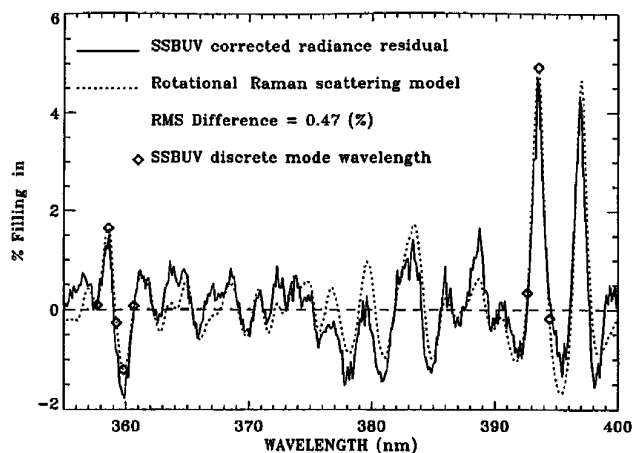


Fig. 11. Observed filling in,  $k^{\text{ob}}$  (or corrected radiance residual, solid curve), from the average of two SSBUV sweep mode scans with an average solar zenith angle of  $87.5^\circ$ , and computed percent filling in,  $k^{\text{c}}$  (dotted curve), as a function of wavelength.

the filling in that would be observed when the Earth radiance scan is shifted  $0.02 \text{ nm}$  with respect to the solar irradiance scan, denoted by  $k_{\Delta\lambda_0}$  (dotted curve). In Fig. 10,  $k_{\Delta\lambda_0}$  appears to be shifted from  $k^{\text{c}}$  by  $\sim 0.2 \text{ nm}$ . The magnitude of  $k_{\Delta\lambda_0}$  is also greater than that of  $k^{\text{c}}$  near the peaks of  $k^{\text{c}}$ .

Figure 11 shows the observed filling in,  $k^{\text{ob}}$  (solid curve), from the average of two continuous sweep scans, both taken at high solar zenith angles and under relatively cloud-free conditions (reflectivities less than 25%). Also shown in Fig. 11 is the computed filling in,  $k^{\text{c}}$  (dotted curve). Good agreement is seen between the observed and computed filling in, with an rms difference of  $\sim 0.5\%$  and a correlation of 0.88. As described above, most of the difference between the observed and computed filling in is due to the inability to correct completely for scene changes. Other differences may be due to the presence of an additional absorber such as collisionally induced absorption by  $\text{O}_2\text{-O}_2$ , which has bands at  $360.5$  and  $380.2 \text{ nm}$ . The peak effect on radiances at these two wavelengths was computed by the use of cross sections from Greenblatt *et al.*<sup>23</sup> The  $\text{O}_2\text{-O}_2$  absorption is a function of solar zenith angle and varies between  $0.65\%$  and  $0.91\%$  at  $360 \text{ nm}$  and between  $0.32\%$  and  $0.48\%$  at  $380 \text{ nm}$ . The bands are relatively broad, with a FWHM of  $4.8 \text{ nm}$  at  $360.5 \text{ nm}$  and a FWHM of  $4.4 \text{ nm}$  at  $380.2 \text{ nm}$ . Anomalous features, such as the peak at  $388 \text{ nm}$ , occurred in only one of the scans. The cause of these spurious features is unknown. Also shown in Fig. 11 are the wavelengths of the discrete mode SSBUV observations, which are discussed below.

#### B. Solar Zenith Angle Dependence

The SSBUV instrument was programmed to make RRS measurements in the discrete mode during two separate experiments on the STS-62 flight in March 1994. The objective of these experiments was to make many high-accuracy measurements of the filling in in order to establish its dependence on solar

zenith angle and cloud effects. The first experiment involved scanning the instrument back and forth repeatedly over three wavelengths centered around the Ca II K line near  $393 \text{ nm}$ , as shown in Fig. 11. Observations at these wavelengths were obtained during one orbit. In the second experiment, the instrument was scanned back and forth over the five wavelengths near  $360 \text{ nm}$  and was scanned once over the three Ca II K line wavelengths. Observations were made by the use of this wavelength pattern over four orbits.

As shown in Fig. 11, three of the selected wavelengths ( $393.53$ ,  $359.82$ , and  $358.62 \text{ nm}$ ) occurred at a positive or negative peak in the RRS spectrum. The remaining wavelengths ( $394.42$ ,  $392.63$ ,  $360.67$ ,  $359.26$ , and  $357.70 \text{ nm}$ ) were chosen such that each RRS peak wavelength was bracketed by two wavelengths at which the filling in was negligible (i.e., continuum). The filling-in factor is approximately equal to the normalized radiance at the peak wavelength divided by the average normalized radiance of the two continuum wavelengths. Because the scene can change significantly over the  $6 \text{ s}$  required to make three discrete wavelength observations, it was necessary again to correct for the scene changes caused by changing solar zenith angle and reflectivity. To account for scene changes, we divided the normalized radiance at each discrete wavelength by the coincident CCR radiance. Computing  $k^{\text{c}}$  in this way cancels out any effects that are approximately linear with wavelength over the small wavelength range of the three discrete observations.

In Fig. 12, the observed filling in is shown as a function of solar zenith angle for each of the three peak wavelengths. The data were screened so that only relatively cloud-free scenes (reflectivities less than 25%) were included. Data points in Fig. 12 represent the mean filling in averaged over  $5^\circ$  solar zenith angle bins. Error bars represent the standard error of the mean. There were approximately 25 data points per bin. Also shown in Fig. 12 is the theoretically predicted filling in, which was computed

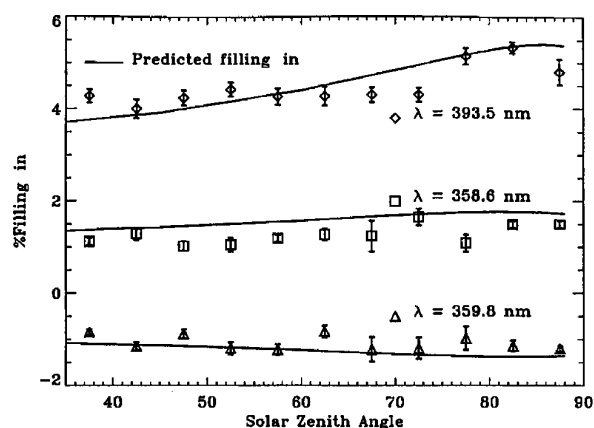


Fig. 12. SSBUV observed mean filling in as a function of solar zenith angle at  $393.5$ ,  $359.8$ , and  $358.6 \text{ nm}$ , with error bars indicating the standard error of the mean obtained in relatively cloud-free conditions (reflectivities  $< 25\%$ ).

at a surface pressure of 1 bar and a reflectivity of 8%. The predicted filling in agrees with the observed filling in at 359.8 nm to within the accuracy of the measurements. However, at 358.6 nm there appears to be an offset between the predicted and observed filling in. At 393.5 nm it is unclear if the solar zenith angle dependence of the model agrees with the observations.

We used continuous scan data from the SBUV instrument to examine further the solar zenith angle dependence of the filling in. Figure 13 shows the observed and predicted filling in at wavelengths similar to those used in the SSBUV discrete measurements. The exact wavelengths used were 394.52, 393.52, 392.52, 360.74, 359.94, 359.14, 358.54, and 357.94 nm. One reduces the noise in the SBUV data by averaging over a large number of points in each bin (approximately 700 points per bin). The SBUV measurements were also made at solar zenith angles down to 0°. The dotted curve in Fig. 13 is the predicted filling in multiplied by an empirical offset value of 1.05. It is apparent that even though the observed filling in differs from the predicted filling in by a constant factor at both wavelengths near 360 nm, the solar zenith angle dependence agrees quite well at these wavelengths. However, at 393.5 nm, the solar zenith angle dependence of the observed filling in appears to deviate from the predicted filling in at solar zenith angles greater than ~40°.

Figure 14 shows the ratio of the filling in observed with the SSBUV instrument to that observed with the SBUV instrument. The offsets are due to the use of slightly different wavelengths. The ratios appear to be relatively constant with solar zenith angle at all three wavelengths. Because the same effects are seen in two different instruments operating in two different modes, the difference between the observed and computed filling in at 393.5 nm is not likely to be due to an instrumental effect. The

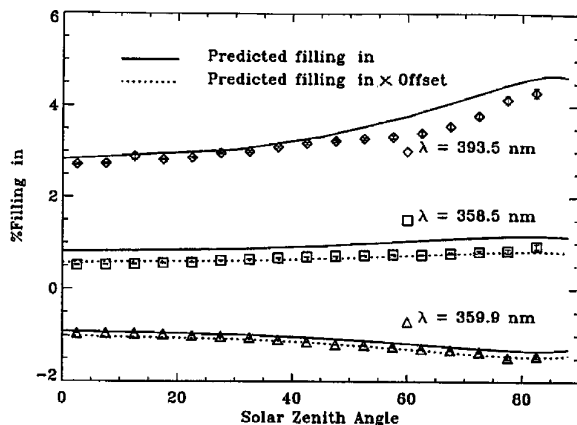


Fig. 13. SBUV observed mean filling in as a function of solar zenith angle at 393.5, 359.9, and 358.5 nm, with error bars indicating the standard error of the mean obtained in relatively cloud-free conditions (reflectivities <25%). Solid curves are the computed filling in, and the dotted curves are the computed filling in multiplied by an empirical offset.

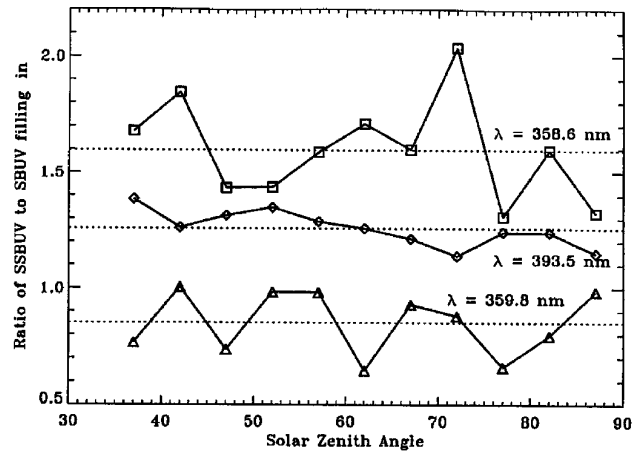


Fig. 14. Ratio between filling in observed with the SSBUV and SBUV instruments as a function of solar zenith angle (solid curves) for 393.5, 359.9, and 358.5 nm. Dotted lines are the ratios averaged over all solar zenith angles.

difference between the observed and computed Ring effect near the 60° solar zenith angle at 393 nm is not understood.

Although in our model we do not explicitly consider Mie scattering in the atmosphere, previous calculations have shown that at non-ozone-absorbing wavelengths, the effect of aerosol scattering on the buv radiances can be modeled accurately by the use of the concept of Lambert-equivalent reflectivity (Bhartia *et al.*<sup>24</sup>). In this concept one accounts for Mie scattering by increasing the surface reflectivity in the simple Rayleigh model we described above. Observations made with the TOMS instrument on the Nimbus-7 satellite indicate that this simple concept works well in most cases in predicting the wavelength dependence of spectral radiance in the 310–380 nm range. It is possible that the effect of Mie scattering on RRS cannot be modeled so simply. However, it is hard to understand why such an effect would show up at 393 nm and not at other wavelengths.

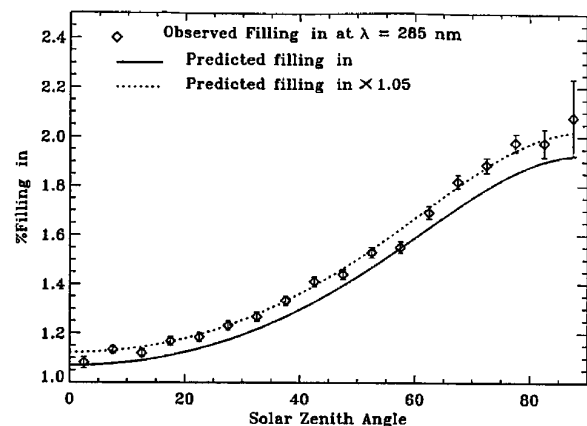


Fig. 15. SBUV observed mean percent filling in as a function of solar zenith angle at 285 nm. The solid curve is the computed single-scatter filling in and the dotted curve is the computed filling in multiplied by an empirical offset.

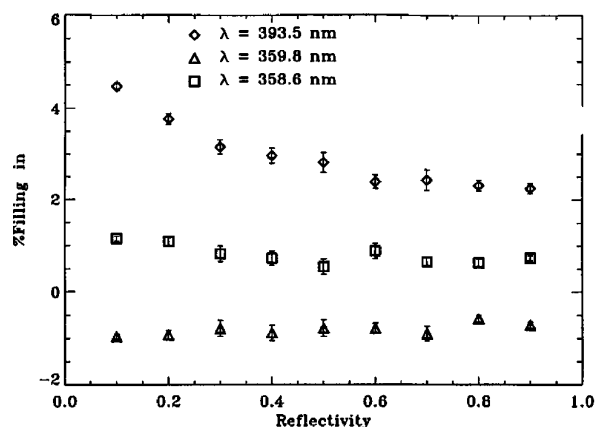


Fig. 16. SSBUV observed mean percent filling in as a function of reflectivity at 393.5, 359.8, and 358.6 nm, with standard error bars for solar zenith angles between 35° and 70°.

Finally, to verify Eq. (1), we examine the filling in at wavelengths short of 290 nm, where most of the observed backscattered radiation is due to single scattering. The solar zenith angle dependence of RRS comes primarily from  $1 - f_0$  in Eq. (1), which depends on the first order of scattering in the atmosphere. Figure 15 shows the observed filling in at the Mg I line near 285 nm as a function of  $\theta_0$  averaged over 10° solar zenith angle bins. The solid curve is the theoretically predicted filling in, and the dotted curve is the predicted filling in times 1.05. There were approximately 2000 separate observations in each bin, which greatly increased the signal-to-noise ratio of the binned averages over that of a single observation. Although there appears to be a 5% offset between the predicted and observed filling in, the solar zenith angle dependence of the observed filling in agrees very well with the predicted filling in.

### C. Cloud Effects

In Fig. 16 the observed filling in at the SSBUV discrete mode wavelengths is shown as a function of reflectivity for solar zenith angles between 35° and 70° (the solar zenith angle dependence over this range is small). Data points indicate the mean filling in averaged over reflectivity bins of 0.1 or 10%, with error bars representing the standard error of the mean. Similar results were observed in SBUV continuous scan data. As expected, the observed filling in decreased with increasing reflectivity. An increase in reflectivity may be interpreted as an increase in cloud fraction. A qualitative comparison of the observations with model predictions will not be made here, as individual observations depend on the cloud height and solar zenith angle. A detailed study of cloud effects on RRS filling in has been made by Joiner and Bhartia.<sup>25</sup>

### 5. Conclusions and Future Research

Good agreement was obtained between our model of buv rotational Raman filling in and the filling in observed with both the SSBUV and SBUV instru-

ments. The spectral characteristics of our model agree well with the observations. The dependence of the RRS model on solar zenith angle agrees well with the observed filling in in the case of single scattering. The observed solar zenith angle dependence of the observed filling in agrees in general with that predicted by our model in the case of multiple scattering, although some small differences were seen. We have also shown that, as expected, the magnitude of the filling in decreases in the presence of clouds.

The type of analysis presented here can be also be applied to shorter wavelengths, which are sensitive to ozone absorption. It may be possible to detect small errors in forward radiative transfer calculations after RRS has been accounted for. The rotational Raman-scattering model will also be used to derive an RRS radiance correction that will be applied to TOMS and SBUV ozone-retrieval algorithms.

The authors thank the entire SSBUV team, especially P. DeCamp, T. Kelly, K. Laaman, and J. Leitch, as well as personnel at International Development and Energy Associates, Inc., for operations and assistance in obtaining and processing the SSBUV data. We also thank T. Swissler and J. Gleason for helpful discussions.

### References

1. J. F. Grainger and J. Ring, "Anomalous Fraunhofer line profiles," *Nature* **193**, 762 (1962).
2. A. W. Harrison and D. J. W. Kendall, "Fraunhofer line filling in (3855–4455 Å)," *Can. J. Phys.* **52**, 940–944 (1974).
3. A. W. Harrison, "Diurnal variation of the Ring effect," *Can. J. Phys.* **54**, 1000–1005 (1975).
4. F. E. Barmore, "The filling-in of Fraunhofer lines in the day sky," *J. Atmos. Sci.* **32**, 1489–1493 (1975).
5. L. Wallace, "Rayleigh and Raman scattering by H<sub>2</sub> in a planetary atmosphere," *Astrophys. J.* **176**, 249–257 (1972).
6. R. T. Brinkman, "Rotational Raman scattering in planetary atmospheres," *Astrophys. J.* **154**, 1087–1093 (1968).
7. W. D. Cochran, L. Trafton, W. Macy, and J. H. Woodman, "Raman scattering in the Jovian atmosphere," *Astrophys. J.* **247**, 734–740 (1981).
8. M. J. Price, "On probing the outer planets with the Raman effect," *Rev. Geophys. Space Phys.* **15**, 227–234 (1977).
9. G. W. Kattawar, A. T. Young, and T. J. Humphreys, "Inelastic scattering in planetary atmospheres. I. The Ring effect, without aerosols," *Astrophys. J.* **243**, 1049–1057 (1981).
10. S. Solomon, A. L. Schmeltekopf, and R. W. Sanders, "On the interpretation of zenith sky absorption measurements," *J. Geophys. Res.* **92**, 8311–8319 (1987).
11. H. Park, D. F. Heath, and C. L. Mateer, "Possible application of the Fraunhofer line filling-in effect to cloud height measurements," in *Meteorological Optics*, 1986 OSA Technical Digest Series (Optical Society of America, Washington, D.C., 1986), pp. 70–81.
12. A. T. Young, "Rayleigh scattering," *Appl. Opt.* **20**, 533–535 (1981).
13. D. R. Bates, "Rayleigh scattering by air," *Planet. Space Sci.* **32**, 785–790 (1984).
14. C. M. Penney, R. L. St. Peters, and M. Lapp, "Absolute rotational Raman cross sections for N<sub>2</sub>, O<sub>2</sub>, and CO<sub>2</sub>," *J. Opt. Soc. Am.* **64**, 712–716 (1974).
15. G. J. Rottman, T. N. Woods, and T. P. Sparr, "Solar-stellar irradiance comparison experiment 1. 1. Instrument design and operation," *J. Geophys. Res.* **98**, 10667–10677 (1993).

16. T. N. Woods, G. J. Rottman, and G. J. Ucker, "Solar-stellar irradiance comparison experiment 1. 2. Instrument calibrations," *J. Geophys. Res.* **98**, 10679–10694 (1993).
17. J. V. Dave, "Multiple scattering in a non-homogeneous, Rayleigh atmosphere," *J. Atmos. Sci.* **22**, 273–279 (1964).
18. J. J. DeLuisi and C. L. Mateer, "On the application of the optimum statistical inversion technique to the evaluation of Umkehr observations," *J. Appl. Meteorol.* **10**, 328–334 (1971).
19. T. R. Caudill, "Accuracy of the Total Ozone Mapping Spectrometer algorithm at polar latitudes," Ph.D. dissertation (University of Arizona, Tucson, Ariz., 1994).
20. R. D. McPeters, "Climatology of nitric oxide in the upper stratosphere, mesosphere, and thermosphere: 1797 through 1986," *J. Geophys. Res.* **94**, 3461–3472 (1989).
21. E. Hilsenrath, R. P. Cebula, R. Caffrey, and S. Hynes, "Implications of space shuttle flight on the calibration of instruments observing atmospheric ozone and the solar irradiance," *Metrologia* **28**, 301–304 (1991).
22. R. P. Cebula, E. Hilsenrath, and B. Guenther, "Calibration of the Shuttle borne Solar Backscatter Ultraviolet Spectrometer," in *Optical Radiation Measurements II*, J. M. Palmer, ed., *Proc. Soc. Photo-Opt. Instrum. Eng.* **1109**, 205–218 (1989).
23. G. D. Greenblatt, J. J. Orlando, J. B. Burkholder, and A. R. Ravishankara, "Absorption measurements of oxygen between 330 and 1140 nm," *J. Geophys. Res.* **95**, 18577–18582 (1990).
24. P. K. Bhartia, J. Herman, R. D. McPeters, and O. Torres, "Effect of Mount Pinatubo aerosols on total ozone measurements from backscatter ultraviolet (BUV) experiments," *J. Geophys. Res.* **98**, 18547–18554 (1993).
25. J. Joiner, and P. K. Bhartia, "Determination of cloud pressures using rotational Raman scattering in satellite backscatter ultraviolet measurements," Submitted to *J. Geophys. Res.*